RSC
Applied Interfaces

ROYAL SOCIETY
OF CHEMISTRY

PAPER

View Article Online
View Journal | View Issue

Cite this: *RSC Appl. Interfaces*, 2026, 3, 551

Novel fast synthesis route for α-MgAgSb thermoelectric materials

Beatriz A. Santos, *[a] Ana I. de Sá,[b] Paulo Luz,[b] Filipe Neves, [b]
Johannes de Boor [cd] and António P. Gonçalves [a]

Thermoelectric (TE) materials capable of waste heat recovery in the temperature range of 300–525 K remain relatively underdeveloped compared to conventional Bi_2Te_3-based systems, which present inherent environmental, health, and cost challenges. Recently, MgAgSb-based compounds have garnered significant research interest for applications in this temperature range owing to their intrinsically low thermal conductivity, high figure of merit and higher abundance. However, synthesis of the desired low-temperature α-MgAgSb phase typically requires highly controlled production processes—such as multi-step mechanical alloying, followed by extensive, week-long annealing—to mitigate the formation of or transition to undesirable phases. This study proposes an original, rapid, and scalable synthesis strategy combining induction melting for only six minutes with the subsequent classic hot-pressing method. We investigated the effect of nominal stoichiometry on thermoelectric performance by synthesising three distinct compositions: $MgAg_{0.97}Sb_{0.995}$, $MgAg_{0.965}Sb_{0.985}$, and $MgAg_{0.955}Sb_{0.985}$. The $MgAg_{0.955}Sb_{0.985}$ composition exhibited optimal performance, achieving an average power factor (PF) of 12.8 μW K^{-2} cm^{-1} in the 300–525 K range. By considerably reducing the thermal budget and processing time, this approach significantly improves the energy payback time (EPBT) and reduces the carbon footprint of production, addressing the critical sustainability-performance trade-off that limits large-scale deployment. This result validates the capacity of the proposed fast synthesis route to yield performant MgAgSb-based samples and suggests that the optimal nominal composition is dependent on the specific production technique employed. Fundamentally, this work demonstrates the rapid and successful preparation of the desired α-MgAgSb phase using an easily scalable technique that does not require a perpetually inert atmosphere. This process utilises bulky precursor elements directly, significantly reducing production complexity, associated costs, and health hazards. This advancement provides a simpler and more industrially viable pathway for the transition of MgAgSb materials toward commercial availability.

Received 23rd December 2025,
Accepted 30th January 2026

DOI: 10.1039/d5lf00400d

rsc.li/RSCApplInter

1. Introduction

Thermoelectric materials have attracted considerable interest owing to the increase in global energy needs and the implementation of new sustainability policies. These materials have the ability to convert thermal energy into electrical energy (and *vice versa*), offering several advantages, such as the absence of moving parts, noise or vibrations, adaptability to different temperature ranges and designs, low maintenance and high durability.[1] These characteristics, along with the possibility of generating energy from waste heat and employing solid-state electric cooling, have put them in the spotlight as a promising solution to help alleviate the global energy crisis.

Regardless of their vast application potential and numerous advantages, thermoelectric materials face some challenges, the primary limitation being their lower efficiency (*e.g.*, compared to photovoltaic systems) close to room temperature, which typically remains below ~10%.[2,3] This is partially because the relevant material parameters are interdependent, making performance optimization a complex task.[4] A metric used to evaluate the performance of a thermoelectric material is the dimensionless figure of merit (zT), which is defined using the following equation:

$$zT = \frac{S^2\sigma}{\kappa_{el} + \kappa_{lat}} T \tag{1}$$

where S is the Seebeck coefficient, σ is the electrical conductivity, κ_{el} and κ_{lat} are the electronic and lattice contributions to thermal conductivity, respectively, and T is

---

[a] CeFEMA, Campus Tecnológico e Nuclear, Instituto Superior Técnico, Universidade de Lisboa, Estrada Nacional 10, km 139.7, Bobadela, Portugal.
E-mail: beatriz.santos@ctn.tecnico.ulisboa.pt
[b] Laboratório Nacional de Energia e Geologia (LNEG), Estr. Paço do Lumiar 22, 1600-038 Lisboa, Portugal
[c] German Aerospace Center (DLR), Institute for Frontier Materials on Earth and in Space, Linder Höhe, 51147 Köln, Germany
[d] University of Duisburg-Essen, Faculty of Engineering, Institute of Technology for Nanostructures (NST) and CENIDE, 47057 Duisburg, Germany

the absolute temperature. It is generally considered that a good thermoelectric material has a zT value around 1,[5] but the higher the better.

Different materials have been studied over the years to identify those suitable for operation in the 288 K to 453 K temperature range, for close-to-room temperature applications. To date, virtually all commercially available thermoelectric devices are based on Bi_2Te_3 materials.[6] These materials were discovered in the 1950s and display a zT ~1.[1,7] However, a fundamental issue remains: Bi_2Te_3 contains toxic, rare and expensive materials, and its performance is improved by doping with Se, Sb and/or Pb,[8,9] the last being highly restricted in the European Union (Directive 2011/83/EU). All this makes Bi_2Te_3 an unattractive option for sustainable energy applications.

Among potential alternatives to Bi_2Te_3-based materials, the magnesium-based p-type MgAgSb compound is a strong candidate due to its greater sustainability and high performance in this temperature range, displaying $zT > 1$ and efficiencies of ~8.5%.[10] This compound possesses three distinct phases, α, β and γ, depending on the temperature, and each phase displays quite different thermoelectric properties.[11]

The room-temperature α-MgAgSb phase is stable up to ~563 K. Above this, it transforms first into the intermediate β-phase, which is stable until ~633 K, and beyond that temperature, it transforms into the γ-phase, which persists up to ~693 K and decomposing above it.[12,13] One of the main problems of this material is that, after being formed, the γ-phase remains in the material even when cooled to room temperature, worsening the thermoelectric performance of MgAgSb.[12,14]

Ergo, it is important to understand the particularities of this material. 1) – The α-phase is the one with interesting thermoelectric properties, exhibiting a high power factor coupled with an intrinsic low thermal conductivity, which is associated with the weak chemical bonding between the same elements (longer bond lengths), resulting in low sound velocity and low thermal conductivity.[15,16] 2) – The crystal structure distortion (tetragonal geometry) allied with the presence of high anharmonicity of α-MgAgSb, as well as the low frequency of optical phonons, leads to low thermal lattice conductivity.[17–19] 3) – The p-type behaviour of the MgAgSb compound derives from the intrinsic Mg and Ag point defects, with the dominant ones being Ag vacancies (V_{Ag}) and Ag occupying the Mg sites (Ag_{Mg}), due to their lower formation energy, in comparison with Mg_{Ag} antisites. 4) – An increase in the number of band valleys close to the Fermi level that improves the thermoelectric performance.[20,21]

Several studies and attempts to improve the thermoelectric performance of α-MgAgSb have been made over the past decade, mainly using strategies, such as doping, band engineering and manipulation of intrinsic point defects, by optimizing production conditions and methods.[20,22–24] Accordingly, changes in sintering conditions greatly affect the concentration and mobility of charge carriers through intrinsic point-defect engineering, while additionally tuning the phonon scattering.[23]

A further challenge is that while the α-phase is the most desirable for thermoelectric applications, it is rather difficult to synthesize it as a single phase due to the recurrent presence of the γ-phase and other impurities such as dyscrasite (Ag_3Sb), antimony (Sb) and magnesium antimonide (Mg_3Sb_2).

Samples with higher contents of dyscrasite tend to exhibit a minor decrease in the Seebeck coefficient, while greatly increasing the electrical conductivity and charge carrier concentration. In contrast, an increasing fraction of magnesium antimonide leads to a noticeable decrease in electrical conductivity, reaching an order of magnitude below its maximum, while slightly increasing the Seebeck coefficient. This results in a more favourable region of the phase ternary diagram near Ag_3Sb than towards Mg_3Sb_2. Nevertheless, the ideal composition is presumably around $MgAg_{0.97}Sb_{0.995}$, where the best balance between all the thermoelectric properties is achieved.[25]

Liu *et al.*[22] achieved a maximum zT of ~1.4 at 550 K (average zT of ~1.1), with the $MgAg_{0.97}Sb_{0.99}$ nominal composition by optimizing the hot-pressing conditions at 533 K, reaching a compromise between the decrease in carrier concentration, rise of carrier mobility and lowering of thermal conductivity. Further investigations regarding the composition of the undoped MgAgSb were performed by the same group, concluding that an optimized composition of $MgAg_{0.97}Sb_{0.995}$ could significantly enhance the power factor.[26] Onwards, this was the adopted composition for most groups researching the MgAgSb-based materials. Nevertheless, a recent article by Zhang *et al.*[27] suggests that a stoichiometry without Ag or Sb deficiencies and a highly controlled multi-step process—ball-milling (BM), spark plasma sintering (SPS) and annealing—can lead to a better performance of α-MgAgSb, achieving an average zT of 1.4 (300–573 K). This study highlights the critical importance of the selection of material processing methods to acquire the desired properties (large grains, high carrier mobility) and enhance the performance of tricky materials, such as α-MgAgSb.

Conventional synthesis routes for MgAgSb are typically the solid-state reaction and high-energy ball milling (mechanical alloying), which are reliable but very time-consuming. As an alternative, an innovative preparation method using induction melting for MgAgSb-based materials was developed. This work aimed to establish an efficient, simple, quick, and consistent production method for high-performance MgAgSb-based thermoelectric materials. Indeed, the induction-melting approach enabled the rapid and reproducible synthesis of MgAgSb in just 6 minutes, something that had not been achieved previously.

2. Experimental procedure

Since the Ag_3Sb phase is an impurity that affects thermoelectric performance, and Mg losses during the process (*e.g.*, during induction melting and hot-pressing) are not negligible, materials with Mg excess, in relation to $MgAg_{0.97}Sb_{0.995}$, were produced, $MgAg_{0.97-x}Sb_{0.995-y}$ (x = 0, 0.005, and 0.015 and y = 0, 0.01). To synthesize these samples, Mg chips 6–35 mesh (99.98% purity from Sigma-Aldrich), Ag pieces, which were cut from a silver foil with 2 mm thickness (99.9% purity from Thermo Scientific) and Sb shots with 6 mm (99.999% purity from Alfa Aesar) were employed.

Graphite sheets with a thickness of 130 μm (99.8% purity, from Alfa Aesar) were used as a lubricant to ease the release of samples during various processing stages.

2.1. Synthesis and sintering methods and conditions

In this study, induction melting was employed to prepare Mg-based materials.

The operating principle of this method is based on a heating process through electromagnetic induction, described by Faraday's law of induction, in which a high-frequency alternating current (AC) passes through a coil. When a conductive material is placed inside this coil, the changing magnetic field induces an eddy current (also known as Foucault current) in the conductor. This eddy current creates a magnetic field in opposition to the original one, causing the conductor to heat up due to its electrical resistance, with the magnitude of the eddy current being directly proportional to the intensity of the magnetic field and inversely proportional to the resistivity of the conductor. A close-up photograph of the coil and conductor of the induction melting furnace is shown in Fig. 1.

The system is cooled by circulating water inside the metallic conductor coil (copper) to ensure that only the crucible and the material to be melted are heated to the desired temperatures, with the other components remaining close to room temperature. To achieve this, a crucible that supports the desired temperatures and allows energy transfer to the material is required.

Induction melting has several advantages over other melting and synthesis methods. It is highly efficient, allowing the heating of only the hot crucible and target material, does not produce pollutants, and operates much faster than traditional techniques. It also allows for precise temperature control and can be easily started or stopped.

Furthermore, the system is easily scalable for industrial applications and many cases, does not require pre-processing of raw materials, in contrast to *e.g.*, ball milling, where a fine granularity of the precursor was identified to be crucial for the final material performance.[28] From an engineering point of view, this is a pivotal feature to move closer to industrial production and market-availability of these TE, ensuring a more sustainable and safe process than working directly with powders, which can set a series of health hazards and environmental concerns.[29,30]

Considering the Life-Cycle Assessment (LCA) of the TE pellets, by cutting down one of the processes in material production from bulk to fine powder,[31] typically, the environmental and health risks are reduced. Particularly for magnesium, the threats of combustion (explosion) and airborne inhalation, which are the main concerns when dealing with magnesium powders, are greatly augmented, requiring working in a glovebox with an inert atmosphere, making the process less practical, time-consuming and expensive.

In the present study, a high emissivity crucible was used to ensure uniform heating. The heating rate was fast enough to limit magnesium sublimation/evaporation, yet sufficiently slow to allow complete fusion of the elements without producing a violent reaction. The synthesis was conducted in a vitreous carbon crucible with a graphite lid and an internal coating of thin graphite foil. The process was carried out under an inert argon atmosphere at 1×10^5 Pa to prevent oxidation. Induction heating (custom-made from Fives Celes) was carefully controlled in three stages: 1) 1118 K, 2) 1163 K, 3) 1198 K, 2 minutes each, which enabled the successful formation of MgAgSb and the mitigation of further

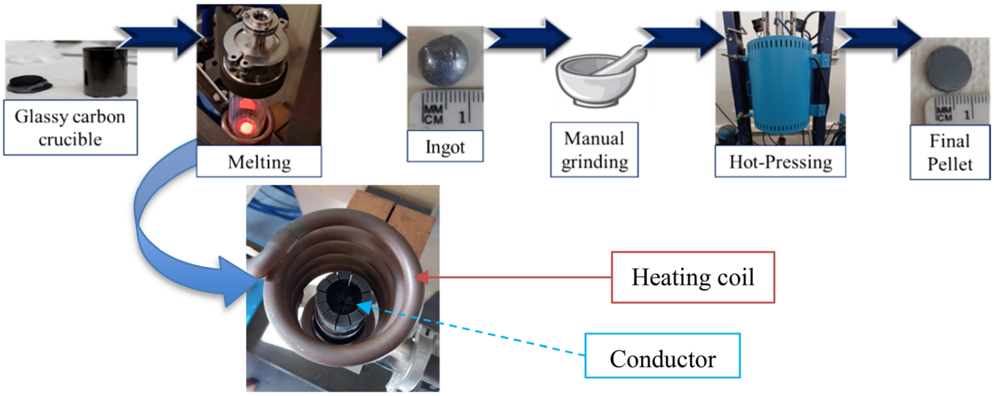

Fig. 1 Representation of the samples' production steps: synthesis and sintering/compaction, with a magnified image depicting the induction coil and conductor. From left to the right: glassy carbon crucible with a graphite lid, where the raw elements (solid pieces) are put inside; melting step in a controlled argon atmosphere; resulting ingot of the sample; manual grinding of the ingot into a powder in an agate mortar; sintering with the compaction step inside a hot-pressing machine (uniaxial pressure) and the final pellet with approximately 10 mm diameter.

magnesium sublimation/evaporation, which always occurs when synthesizing these compounds. This resulted in the production of dense and robust ingots.

Following induction melting, the ingot was manually ground using an agate mortar under ambient conditions until it was reduced to a fine powder. The powder was then placed in a graphite mould with two tantalum pistons and two graphite sheets in between, to ease the removal of the pistons from the pellet. This mould was inserted into a uniaxial hot-press (custom-made from ThermoLab) and sintered for 2 hours at a pressure of 95 MPa and a temperature of 623 K, followed by natural cooling inside the furnace. This final step leads to the formation of the α-phase and reduced the presence of secondary phases formed during the synthesis.

2.2 Analysis and representations

Structural and surface characterization of the samples was made by X-ray diffraction (XRD) and scanning electron microscopy (SEM) coupled with energy dispersive X-ray spectroscopy (EDS), respectively.

The XRD analysis was performed on a D2 PHASEER diffractometer (from Bruker) using a Bragg–Brentano geometry and Cu Kα radiation source (wavelength of 1.54060 nm). All the samples were characterized in a 2θ range from 20° to 80°, with a step size of 0.02° and a time/step of 2 s. These results were then processed using Profex software (version 5.5.) to make Rietveld refinements for each sample and to obtain parameters such as lattice constants and densities. Crystallography Open Database (COD)[32] was used to collect data to build the patterns and Origin Lab (OriginPro 9) for representation of the data.

The SEM/EDS evaluation was performed on a Phenom ProX G6 Desktop SEM equipped with an EDS system (from Thermo Fisher Scientific). Both micrographic acquisition and EDS analysis was carried out using an acceleration voltage of 15 kV at a pressure of 1 Pa. Analysis of the micrographs from SEM were made using ImageJ software (version 1.54p).

All thermoelectric properties of the samples were measured after the initial characterizations, using commercial equipment (LZT, from Linseis), from close-to-room temperature (315 K) to 525 K, with an increase of 5 °C min^{-1}, three consecutive measuring points, with 50 °C intervals, in a helium-controlled atmosphere of 5000 Pa. The Seebeck coefficient and electrical resistivity were directly measured, while the thermal conductivity (k) was calculated from thermal diffusivity, measured using the laser flash method within the equipment, using the relation $k = \rho C_p \alpha$, where ρ, C_p, and α, andare the samples' density, specific heat capacity (at constant pressure) and thermal diffusivity, respectively, with the C_p values calculated using the Neumann–Kopp's law.[33]

3. Results & discussion

3.1. Structural and microstructural characterization

To better evaluate the feasibility of this novel production route of MgAgSb-based compounds, firstly, a general assessment of the samples' morphological microstructure was made by observing the densification of pellets as well as the presence, distribution and concentration of secondary phases throughout the samples. Fig. 2 exhibits SEM micrographs at a magnification of 650× (200 µm in scale) using a backscattered electron detector (BSD) for a), b) and c) images, while a2), b2) and c2) are the corresponding ones using a secondary electron detector (SED), respectively. It should be noted that through SEM micrographs, it is not possible to differentiate between the phases (α, β and γ) of

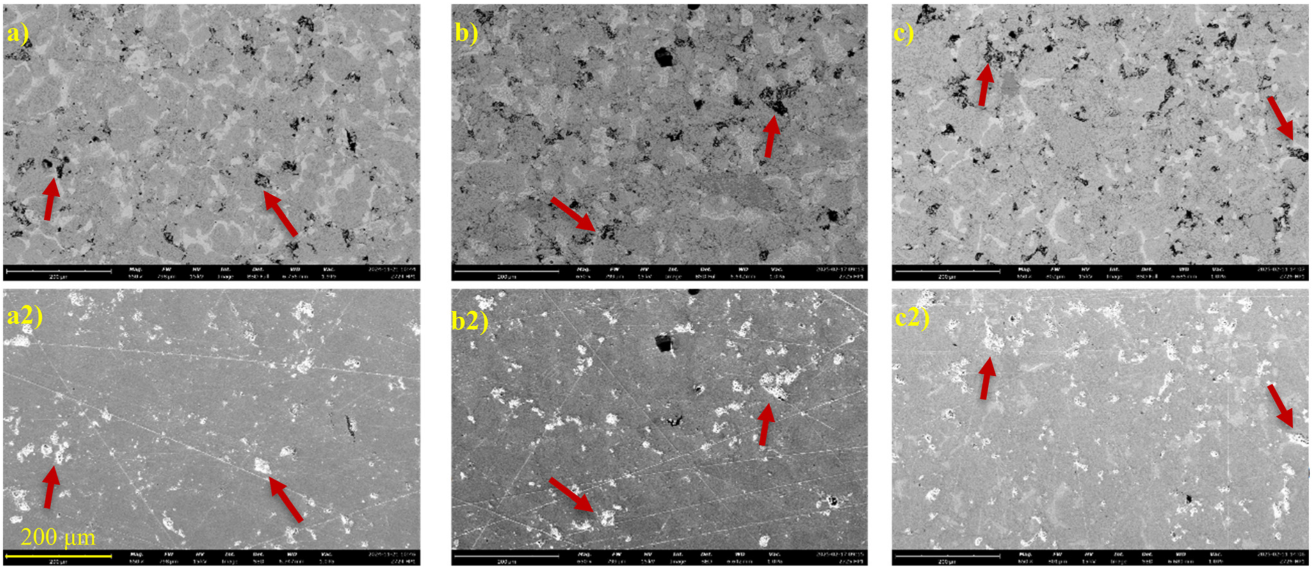

Fig. 2 SEM images of the samples: a) BSD image of $MgAg_{0.955}Sb_{0.985}$, b) BSD image of $MgAg_{0.965}Sb_{0.985}$, c) BSD image of $MgAg_{0.97}Sb_{0.995}$; a2), b2) and c2) are their respective SED images. The arrows in the micrographs indicate examples of "superficial" pores on the samples, with light material underneath.

MgAgSb-based compounds, as all have virtually the same composition.

Observing the micrographs in Fig. 2, the homogeneity, porosity, secondary phases' presence and distribution of samples, as well as a rough estimation of their amount, may be assessed. All samples show good homogeneity within themselves, with the distribution of phases on the surface about the same throughout the different compositions. Additionally, in all samples, the matrix is composed of MgAgSb (further details can be found below), along with a considerable presence of secondary phases, most being displayed as lighter scattered regions (Fig. 2a)–c)), indicating these are mostly composed of heavier elements, than the main matrix, leading to the supposition that these are Ag and Sb rich phases.

It should be noted that most of the pores observed (examples indicated with red arrows) contain lighter material underneath, accordingly being displayed as bright shiny spots on SED micrographs (Fig. 2a2)–c2)), and black spots in BSD. From image and XRD analyses, a good compaction of the pellets was deduced, with relative densities above 90% in all samples.

To estimate Mg losses through the employed production technique, the final and initial weights of the samples were measured. It was assumed that the weight losses were only due to Mg sublimation/evaporation in the process, leading to a ~10 wt% Mg reduction. Further details on the estimation of stoichiometry can be found in the SI section. The presumed actual stoichiometries are shown in Table 1. To simplify, throughout the study, the samples will be denoted by their nominal compositions.

Fig. 3 presents the XRD diffractograms of the studied samples (sintered pellets). The most intense peaks can be indexed to the α-MgAgSb phase, indicating that this is the predominant phase in all samples. However, small peaks pointing to the presence of other phases, such as Ag_3Sb, Sb, Mg_3Sb_2, AgMg and γ-MgAgSb (indicated by arrows), can also be seen. The quantity of each secondary phase according to the Rietveld refinements, as well as the lattice parameters of the main phase, are summarized in Table 1. Additionally, the same analysis for the $MgAg_{0.97}Sb_{0.995}$ sample before the sintering step is also presented.

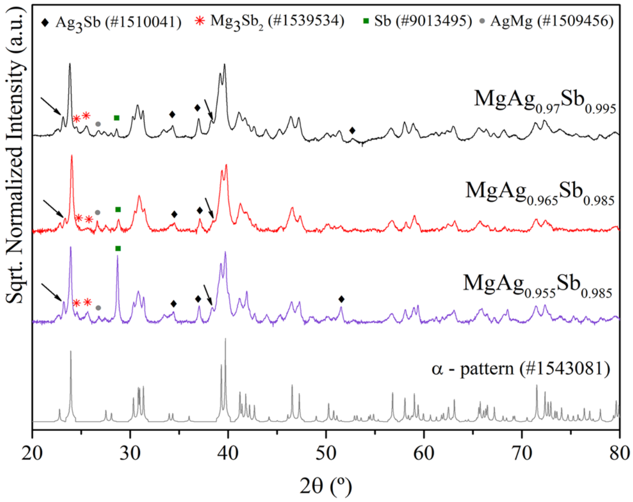

Fig. 3 XRD of the studied samples. Patterns were taken from the Open Crystallography Database (COD).[32] Black diamonds: Ag_3Sb; red stars: Mg_3Sb_2; green squares: Sb; grey circles: AgMg; and black arrows: γ-phase.

The deviations of lattice parameters from the theoretical values,[10] apart from $MgAg_{0.955}Sb_{0.985}$ and $MgAg_{0.97}Sb_{0.995}$ prior to hot-pressing, point towards an expansion of the unit cell, with higher emphasis on the *x* and *y* axes (*a* and *b* parameters have a higher variation than *c*).

Rietveld refinements showed that all sintered samples exhibited less than 5 wt% of γ-MgAgSb. The main secondary phase is dyscrasite, which is observed in all samples with a weight fraction of 10–12% that increases with the Ag content, as expected, whereas the same could not be said for Sb. Indeed, the case of $MgAg_{0.955}Sb_{0.985}$, for which a significant amount of elemental Sb is observed, despite the higher and lower nominal content of Mg and Sb, respectively, is an

Table 1 Crystal structure (lattice parameters) and phase analysis from XRD results and comparison with theoretical calculations for pristine α-MgAgSb. Note that secondary phases with <2 wt% were not considered. The recalculated stoichiometry is obtained by taking into account the Mg loss during the process

	Lattice parameters for α-MgAgSb			
Nominal composition	*a* = *b*	*c*	Secondary phases (wt%)	Recalculated stoichiometry (normalized to one Mg)
$MgAg_{0.955}Sb_{0.985}$	9.1580 ± 0.0004	12.6625 ± 0.0007	4-γ phase 4-Mg_3Sb_2 9-Ag_3Sb 14-Sb	$MgAg_{1.043}Sb_{1.073}$
$MgAg_{0.965}Sb_{0.985}$	9.1909 ± 0.0007	12.7058 ± 0.001	1.4-Mg_3Sb_2 10.5-Ag_3Sb	$MgAg_{1.045}Sb_{1.078}$
$MgAg_{0.97}Sb_{0.995}$	9.1848 ± 0.0005	12.6993 ± 0.0006	5-γ phase 8-Mg_3Sb_2 11-Ag_3Sb	$MgAg_{1.051}Sb_{1.086}$
$MgAg_{0.97}Sb_{0.995}$ (prior hot-pressing)	9.1564 ± 0.0003	12.683 ± 0.0004	23.5-γ phase 21.7-Ag_3Sb 3.4-AgMg	—
Theoretical values MgAgSb (ref. 10)	9.1761 ± 0.0004	12.6960 ± 0.0007	—	—

interesting one. The lower lattice parameters as well as the noticeable amount of elemental Sb appear to be connected to the higher deficiency of Ag, when compared to the other samples.

In order to better understand the formation of different phases, an analysis of the synthesized ingot, after melting and prior to the hot-pressing step, was performed. XRD and SEM/EDS characterization was made using part of the ingot from the sample with a nominal composition of $MgAg_{0.97}Sb_{0.995}$, to evaluate the sequence of phase formation and their quantities. The diffractograms and micrographs are shown in Fig. 4.

In the synthesized ingot, a significant amount of secondary phases is observed in SEM analysis. Dyscrasite (blue target symbol in Fig. 4c) and the γ-MgAgSb phase (identified by XRD) account for approximately 22 wt% and 25 wt%, respectively. By examining Fig. 4c, one can infer the sequence of phase formation. The green dashed rectangle highlights the first phase to solidify, identified as Ag_5Sb. However, this phase subsequently reacts with the melt to form the main phase, MgAgSb (indicated by the purple arrow). Shortly after, MgAgSb also begins to solidify directly from the liquid. Following the formation of MgAgSb, a fine mixture of phases—difficult to clearly distinguish—solidifies, as represented by darker regions in the micrograph. Based on XRD analysis, one of these phases can be attributed to AgMg (black diamond symbol) and another should be MgAgSb, as the Mg_3Sb_2 content is below 1.5 wt%. Finally, Ag_3Sb (blue target symbol) is the last liquid to solidify and appears as the lighter regions in the image. This interpretation is consistent with the secondary-phase distribution presented in Table 1.

What is worth noting is that the phase concentrations change significantly after the hot-pressing step (Table 1), which is particularly evident for the γ-phase. This indicates that, although a considerable amount of γ-phase was initially observed after induction melting, the hot-pressing step can promote the growth of the desired α-phase, almost eliminating the former. Moreover, this demonstrates the crucial role of the sintering method and conditions in phase formation, allowing one to avoid the long thermal treatment (typically lasting several days) usually required when synthesizing α-MgAgSb directly from the three elemental constituents from the start (melting followed by solid-state reaction).[13,23,34]

From the combined observation of secondary phases (*e.g.* Mg_3Sb_2 and Ag_3Sb) from different regions of the Mg–Ag–Sb phase diagram (see Fig. 7), one may deduce that none of the samples has reached thermodynamic equilibrium yet and the observed phases are the result of an interplay between the respective chemical stabilities, the kinetics of diffusion and reaction processes as well as the spatial distribution of different phases.

Starting with the peculiar case of $MgAg_{0.955}Sb_{0.985}$, according to the observations made for the synthesized sample prior to hot-pressing ($MgAg_{0.97}Sb_{0.995}$) and from the formation enthalpies,[21] the MgAgSb phase would be the first to be formed, followed by Mg_3Sb_2 and finally Ag_3Sb. Notwithstanding, if a deficiency in Mg (in relation to the other elements) is present, which is the case in all samples when Mg loss is accounted for, and its nominal value remains the same, this could suggest that all available Mg reacted to form primarily MgAgSb and then Mg_3Sb_2, leaving the excess of Sb to react with Ag, and that is the key

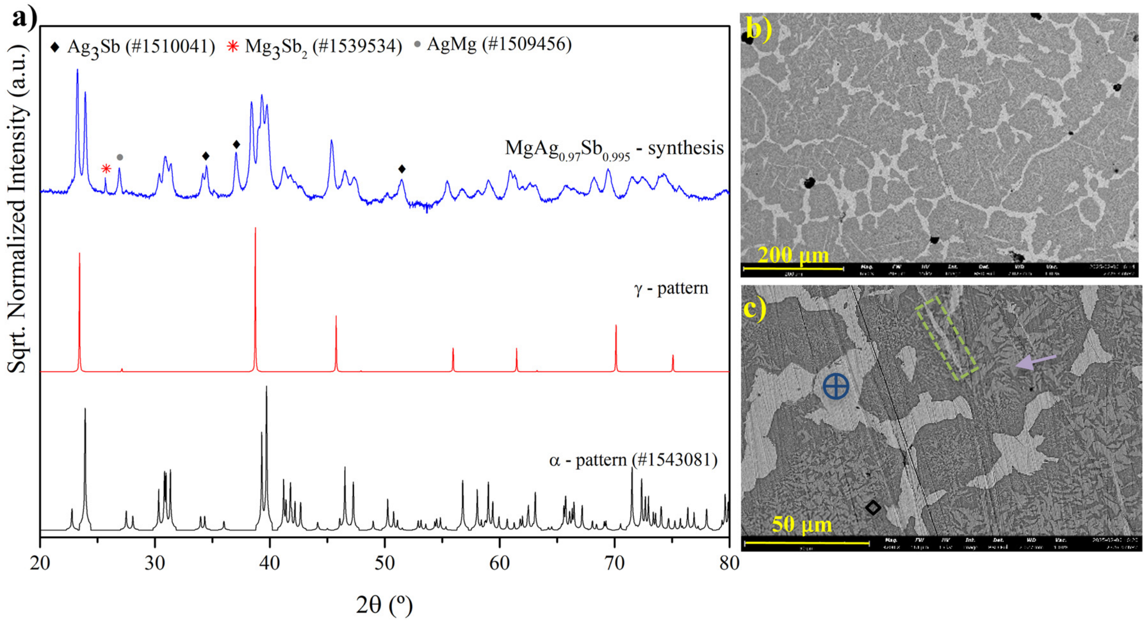

Fig. 4 a) XRD diffractogram of the synthesized $MgAg_{0.97}Sb_{0.995}$ by induction melting, before sintering and compaction. The γ-phase pattern was obtained from literature data;[12] b) micrograph in BSD with a low magnification (200 μm); c) BSD micrograph with a higher magnification (50 μm) and indication of phases: target circle – Ag_3Sb, black diamond – AgMg, traced rectangle – Ag_5Sb, and arrow – MgAgSb.

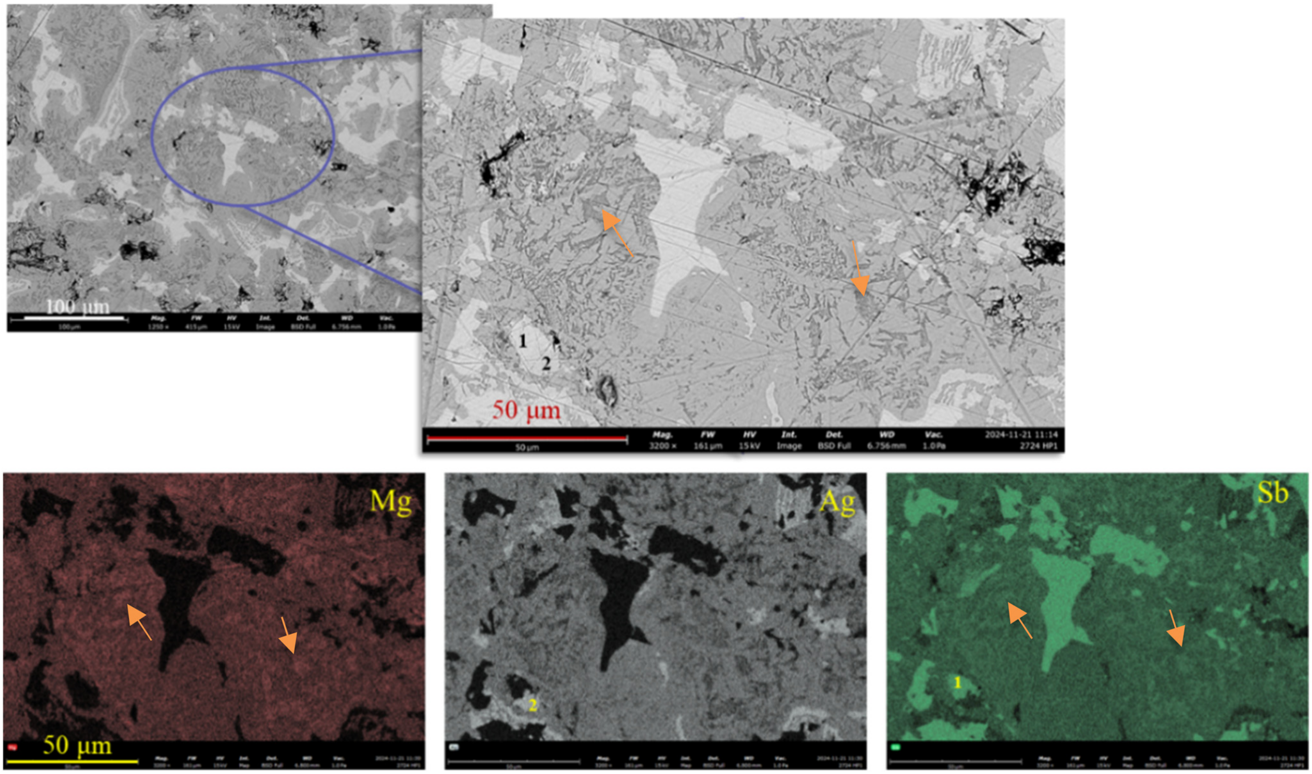

Fig. 5 SEM in BSD with the elemental mapping of $MgAg_{0.955}Sb_{0.985}$. The map analyses were carried out for 5 minutes at 15 kV at a scale of 50 µm. In the BSE image, Ag_3Sb and Sb phases appear to be indistinguishable; however, these phases can be differentiated using EDS elemental mapping, where (1) corresponds to the Sb elemental phase and (2) to the Ag_3Sb phase. Mg_3Sb_2 phase is highlighted with the orange arrows as an example.

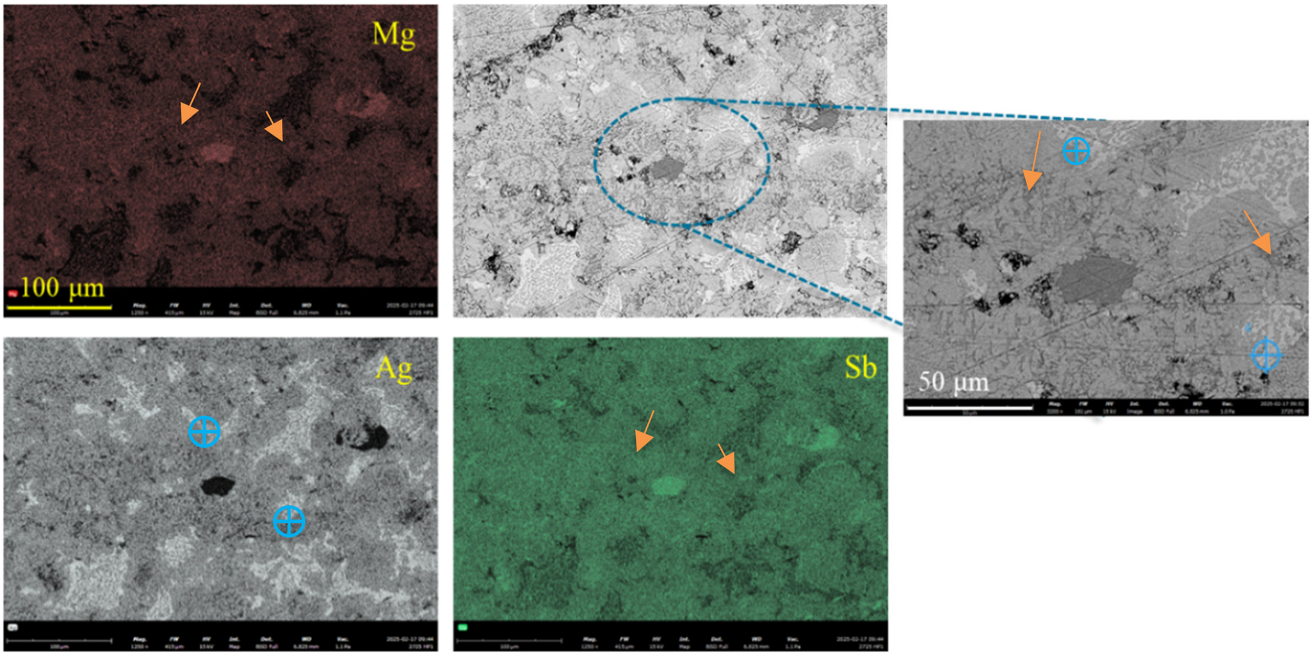

Fig. 6 SEM images in BSD. Larger micrographs: elemental mapping of the sample $MgAg_{0.965}Sb_{0.985}$ at lower magnification (scale 100 µm). The map analysis was carried out for 5 minutes at 15 kV; right side micrograph: higher magnification (50 µm) on a selected region, displaying the behaviour of the secondary phases. Darker grey (arrows) areas are Mg_3Sb_2 phase whereas the lighter areas (target symbol) are Ag_3Sb phase.

parameter here. This sample ($MgAg_{0.955}Sb_{0.985}$) has the lowest Ag concentration and when combined with the formation of Ag_3Sb as a secondary phase shows that a minimum content of Ag is required to avoid sole Sb presence. The purpose of

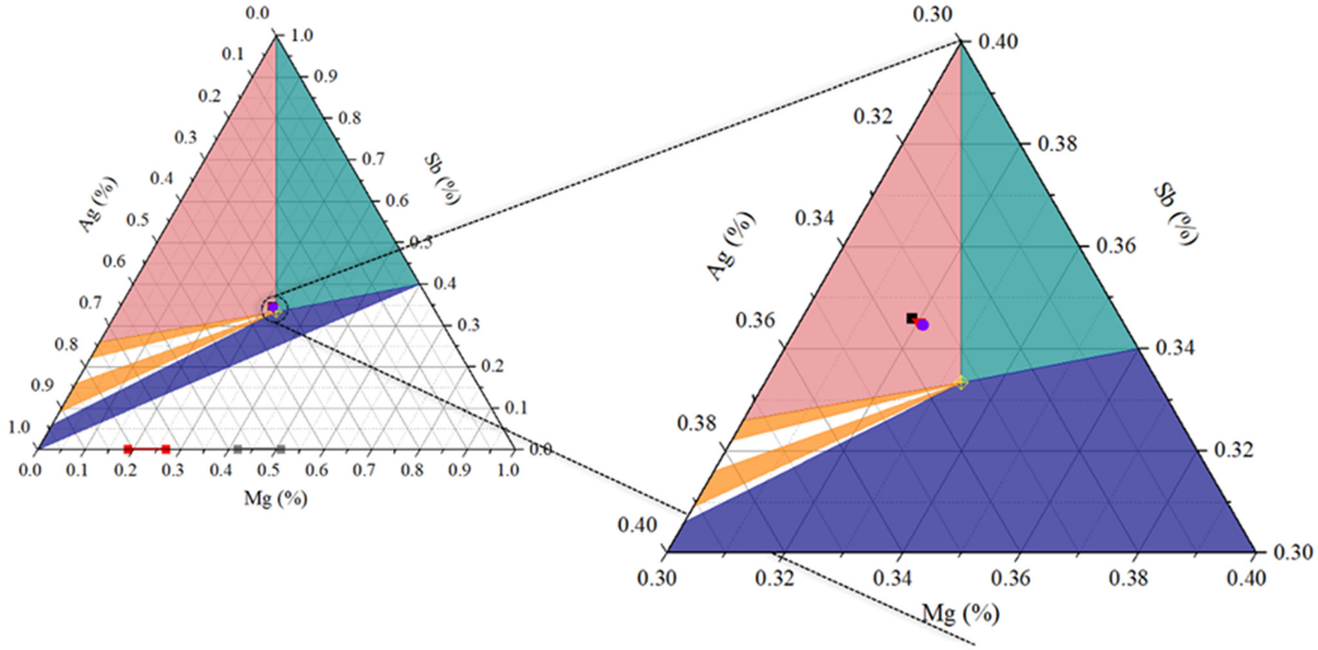

Fig. 7 Mg–Ag–Sb ternary phase diagram at 315 K. Green zone: Mg_3Sb_2 + Sb + MgAgSb; pink zone: dyscrasite (Ag_3Sb) + Sb + MgAgSb; orange zones: dyscrasite-Ag rich + MgAgSb; blue zone: Ag + Mg_3Sb_2 + MgAgSb; grey line: MgAg; and red line: $MgAg_3$. On the right: magnification of the region close to the centre, where the samples are represented in the diagram; $MgAg_{0.97}Sb_{0.995}$ – black square, $MgAg_{0.965}Sb_{0.985}$ – red triangle, and $MgAg_{0.955}Sb_{0.985}$ – purple circle.

studying this composition was to diminish the formation of dyscrasite which, although successfully achieved, lead to other effects, as explained above.

Fig. 5 displays backscattered micrographs and EDS maps of the $MgAg_{0.955}Sb_{0.985}$ sample. It is possible to distinguish the elemental Sb from the Ag_3Sb phases, as well as observe that effectively most elements form the MgAgSb phases, and some part of Mg formed some scattered Mg_3Sb_2 phase (darker grey regions identified with orange arrows).

Sample $MgAg_{0.965}Sb_{0.985}$ showed the lowest content of secondary phases, along with higher deviations of lattice parameters. This might be correlated since a higher strain on the lattice parameters implies a greater capacity of the crystal to accommodate the non-ideal stoichiometric arrangement of atoms, instead of leaving them to form secondary phases outside the main structure.

In Fig. 6, the SEM (in BSD) micrographs and elemental mapping can be observed, with a highlighted region of interest (right side of the figure) to show the distribution of the secondary phases in the sample. In this region, it is clearly visible that the Ag_3Sb phase (blue circles) exhibits a tracery, or scattered, behaviour, similar to what was observed for Mg_3Sb_2 (orange arrows) in the previous sample (Fig. 5). This phenomenon is likely due to a reaction occurring during the hot-pressing step, between these two phases (Ag_3Sb and Mg_3Sb_2), leading to the formation of α-MgAgSb. Therefore, this would suggest that with a stoichiometry with a small deficit of silver, it is possible to diminish the Ag_3Sb phases and increase the fraction of the α-MgAgSb phase.

Fig. 7 exhibits the Mg–Ag–Sb ternary phase diagram[35] near room temperature, highlighting the region close to the MgAgSb stoichiometry and the position of the samples' composition in the diagram according to their recalculated stoichiometry (see Table 1). By studying the position of the samples in the phase diagram and the results observed thus far, one might conclude that these have not reached thermodynamic equilibrium since both Ag_3Sb and Mg_3Sb_2 appear together and are still reacting to form α-MgAgSb. This effect was particularly noticeable for the $MgAg_{0.965}Sb_{0.985}$ sample.

These representations agree well with what was observed in the characterization results, showing that, albeit close to the border with the green area, all samples are in the pink region, where the presence of dyscrasite and Sb is expected. Furthermore, the distribution of these secondary phases creates a complex heterophase interface network, which serves as the primary source of the quantitative scattering effects discussed in the transport analysis in the following section.

3.2. Thermoelectric properties

The thermoelectric properties are represented in Fig. 8, while the average Seebeck coefficient, and electrical and thermal conductivities are given in Table 2, along with charge carrier concentration and charge carrier mobility close to room temperature (315 K). Moreover, a comparison between the performance of these samples with some of the values reported in the literature can be conducted while correlating

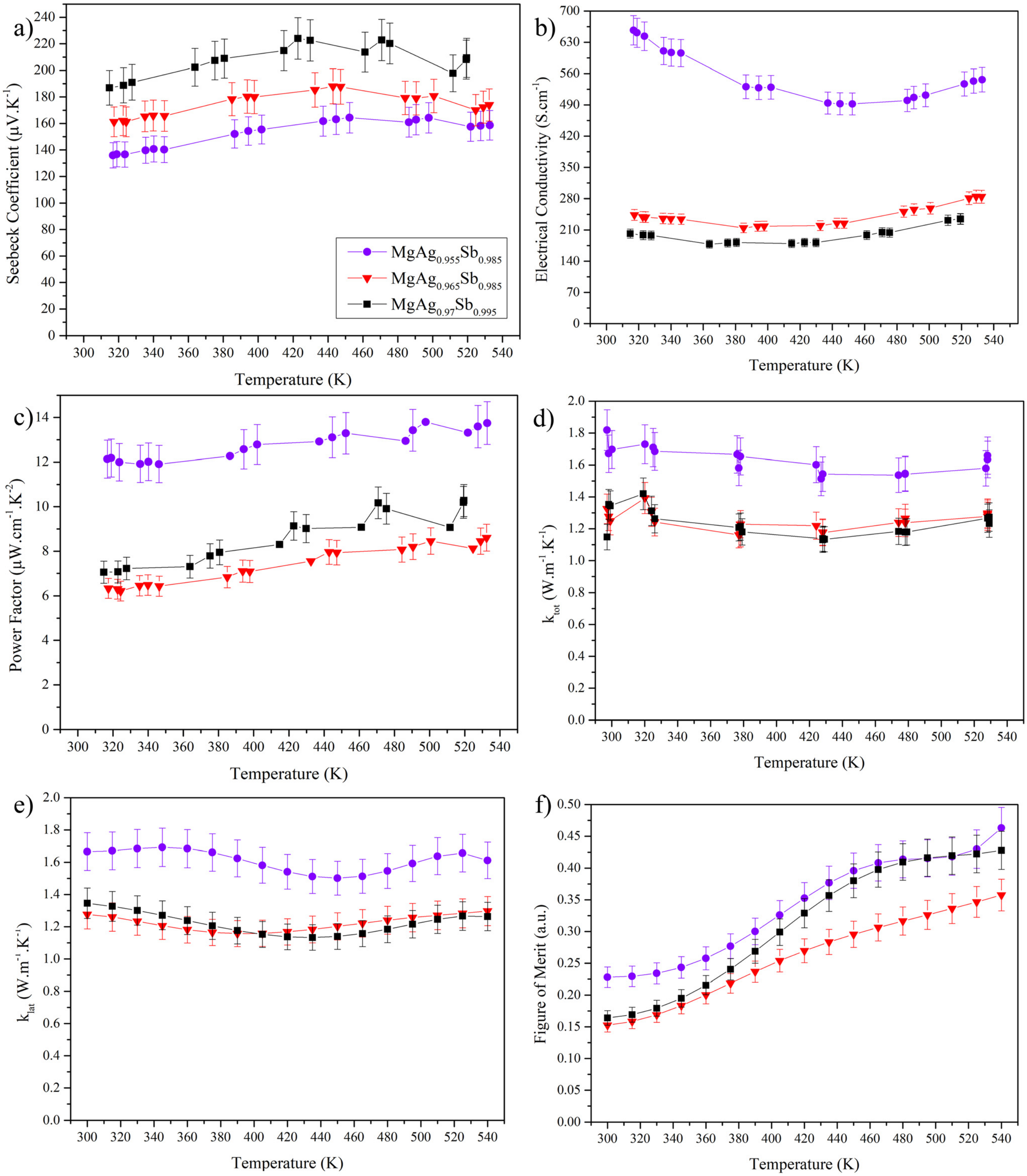

Fig. 8 Thermoelectric properties of the different compositions from 315 K to 525 K: black squares – $MgAg_{0.97}Sb_{0.995}$; red triangles – $MgAg_{0.955}Sb_{0.985}$; and purple circles: $MgAg_{0.955}Sb_{0.985}$. a) Seebeck coefficient; b) electrical conductivity; c) power factor; d) thermal conductivity; e) contribution of lattice thermal conductivity (k_{tot}–k_{el}) and f) figure of merit (zT).

these results with the processing routes and times exhibited in Table 3.

The estimation of the charge carrier was accomplished using the Boltzmann transport theory, and assuming that the bipolar effects are negligible at room temperature, hence just considering that the dominant charge carriers (holes in this case) will contribute to the transport and that scattering by acoustic phonons is dominant.[37,38] Thus, a single parabolic

Table 2 Average values of thermoelectric properties in the temperature range from 315 K to 525 K and charge carrier concentration with the respective mobility for 315 K, along with literature values

Composition	S_{avg} (μV K^{-1})	σ_{avg} (S cm^{-1})	PF$_{avg}$ (μW K^{-2} cm^{-1})	κ_{avg} (W K^{-1} m^{-1})	zT_{avg}	n (10^{19} cm^{-3})	μ (cm^2 V^{-1} s^{-1})
$MgAg_{0.955}Sb_{0.985}$	**154**	**540**	**12.8**	**1.6**	**0.34**	**18.7**	**22**
$MgAg_{0.965}Sb_{0.985}$	177	237	7.4	1.2	0.26	13.8	10.9
$MgAg_{0.97}Sb_{0.995}$	211	197	8.8	1.2	0.31	10.1	12.4
Rodriguez-Barber *et al.*[28]	214	470	20.8	0.81	1.1	6.3	36.4
Back *et al.*[36]	215	568	27	0.90	1.2	8.7	48

Table 3 Comparison between two literature articles and this work, regarding their processing routes, times and Mg outcome

Processing routes/conditions	Time each step	N° steps	Total time	Mg management	Ref.
Two-step BM + SPS/fine powders/all in Ar atmosphere	8 h + 5 h – BM 8 min – SPS	3	~13.13 h	Minimal losses	Rodriguez-Barber *et al.*[28]
Two-step BM + SPS + annealing/all in Ar atmosphere	10 h + 10 h – BM 5 min – SPS 6 h – annealing	4	~26.08 h	Minimal losses	Back *et al.*[36]
IM + HP/chunks/in Ar and air atmosphere	6 min – IM 2 h – HP	2	~2.1 h	~10 wt% Mg losses	**This work**

band model (SPB) can be employed to estimate the carrier concentration, n. It should be noted that the charge carrier concentrations and mobilities were also calculated from literature references, using the same expression, for a higher consistency during comparison.

To calculate n, one must know the Seebeck coefficient (S) and the effective density of states mass (m_D^*), which requires Hall measurements. In the absence of this, and following the same considerations (SPB), one can assume that the value reported by Liu *et al.*[26] for $MgAg_{0.97}Sb_{0.995}$, ($m_D^* = 2.7m_0$, where m_0 is the electron mass) remains approximately the same for all these compositions.

Observing the S and the m_D^* values, it becomes clear that the samples are between a non- and degenerated semiconductor behaviour.[39] According to a recent publication of Novitskii and Mori,[40] eqn (2) is valid for semiconductors that are situated between these regimes. Following the Pisarenko relation between thermopower (S) and charge carrier concentration (n), a scattering factor r must be applied depending on the dominant scattering mechanism, which in this case, was established as being acoustic phonon, hence $r = -1/2$. In the equation, k_B is the Boltzmann constant, T is the temperature, h is the Planck constant and e is the constant elementary charge.

$$S = \frac{k_B}{e}\left[r + \frac{5}{2} + \ln\left(\frac{2(2\pi m_D^* k_B T)^{3/2}}{h^3 n}\right)\right] \tag{2}$$

From the SPB model, one can also determine the carriers' (drift) mobility μ through the relation $\sigma = \mu en$.

Comparing the results obtained in this work (Tables 2 and 3) with the literature, one may observe differences for all compositions in the concentration and mobility of charge carriers, which are higher and lower than the literature values, respectively. In both referred studies (ref. 28 and 36), a two-step synthesis (high-energy ball-milling) was used to ensure the formation of an AgMg precursor before the addition of Sb. This approach is strategically designed to minimize/suppress the formation of Ag_3Sb and Mg_3Sb_2, thereby stabilizing the Mg content and "locking" the desired stoichiometry.

The correlation between the rapid synthesis route and the final thermoelectric properties is driven by the management of intrinsic defects and secondary phases. While the literature employs a two-step ball-milling process to form an AgMg precursor and "lock" the stoichiometry, our 6 minute induction melting route accepts a measured 10 wt% Mg loss, which can be compensated for in future works. This Mg-deficiency acts as a "driving" mechanism for charge carriers. The resulting dyscrasite Ag_3Sb phase and Mg-site vacancies significantly increase the carrier concentration (n) as noted in previous studies. Although the presence of these phases and the rapid cooling rate can hinder grain growth and decrease carrier mobility through enhanced interface scattering, the elevated n compensates for this reduction. This balance allows the $MgAg_{0.955}Sb_{0.985}$ composition to achieve a comparable average power factor of 12.8 μW K^{-2} cm^{-1}. This establishes that the induction melting route provides a distinct transport regime, where high carrier density, rather than ultra-high mobility, sustains competitive performance within a fraction of the time for traditional production.

This distinct transport regime is a direct consequence of the material's defect chemistry. In MgAgSb systems, transport properties are ruled primarily by intrinsic defects, such as vacancies, V_{Ag}, which have a low defect formation energy, and Ag_{Mg} antisites, which also have a lower energy of formation than Mg_{Ag} antisites, particularly in Mg-poor matrices.[23,26] The V_{Ag} and Ag_{Mg} antisites typically act as acceptors (increasing hole concentration) in these systems, thereby diminishing bipolar effects. These defects will tend to increase the charge carrier concentration, enhancing the electrical conductivity in the samples, and reducing the lattice thermal conductivity by increasing the phonon scattering. Albeit, in some cases, depending on the reduced chemical potential, they can work as donor-like, creating the opposite effect.

Besides these intrinsic defects, the charge carrier concentration and mobility are also highly affected by grain boundaries, grain size distribution, porosity and secondary phases. Particularly, the charge carrier mobility serves as a quantitative indicator of the interfacial scattering density.

As shown in Table 2, our samples exhibit mobilities between 10.9 and 22.0 $cm^2\ V^{-1}\ s^{-1}$, representing a ~40–50% reduction compared to the equilibrium-processed samples.[28,36] This deviation is a measurable result of the high density of phase interfaces (specifically Ag_3Sb/α-MgAgSb) and grain boundaries inherent to the rapid induction melting. These incoherent interfaces act as potential barriers that provide significant resistance to electronic transport. Noticeably, this interfacial scattering is non-selective; while it degrades mobility, it concurrently disrupts phonon propagation, maintaining a low lattice thermal conductivity (~1.3 $W\ K^{-1}\ m^{-1}$). Thus, the microstructure essentially functions as a dense network of interfacial filters, trading bulk crystallinity for phonon-glass/electron-crystal behaviour.

The physical origin of these scattering centres is evidenced by the non-negligible presence of secondary phases in the final pellet, along with some grain-size heterogeneity, as it may be observed in the SEM micrographs (Fig. 5 and 6). Both issues can be mostly attributed to the hot-pressing step, since after melting, a dense, large-grain and homogeneous ingot is acquired (Fig. 4). Additionally, this process step can erase the presence of the γ-phase and diminish the amount of Ag_3Sb phases, by triggering further reaction between these and the scattered Mg_3Sb_2, to the desired α-MgAgSb, pointing out that the sintering step has a critical impact on the microstructure and TE behaviour of MgAgSb-based materials.

Based on their nominal stoichiometry, one might expect the sample to contain a high density of V_{Ag}, which aligns with the high determined carrier concentrations, which should improve the thermoelectric properties (usually good TE semiconductors are heavily doped, meaning high *n* (ref. 19)). However, from the recalculated stoichiometries, these are more likely to be Mg-poor samples, with some Sb excess, as it is represented in the ternary diagram (Fig. 7), where all the samples fall into the pink region, where dyscrasite is the dominant secondary phase.

Duparchy *et al.*[35] published a schematic representation, in which different thermoelectric parameters were superpositioned on the ternary Mg–Ag–Sb phase diagram. This diagram was based on experimental results, which enabled a better understanding of the global impact of some specific phases on the properties. Looking at the phase diagram (Fig. 7) and what is reported by Duparchy, in the pink region, where all the samples of this study lay, a higher electrical conductivity and lower Seebeck coefficient, compared to the other regions of the diagram is expected[35] (due to metallic behaviour of dyscrasite), this may indeed be noted (Table 1). Hence, both intrinsic (point defects) and external (secondary phases) effects must be taken into account when deciphering the interplay between them in these samples.

Comparing the data on thermoelectric properties and the XRD results, it is worth noting that a higher presence of secondary phases does not necessarily mean a worse performance. Indeed, we find that the sample with the worst performance was $MgAg_{0.965}Sb_{0.985}$, which exhibited lower amounts of secondary phases, but a higher deviation from the theoretical lattice parameters and a stronger deformation of the crystal structure, which potentially worsens the thermoelectric properties. This is also in agreement with the results from the $MgAg_{0.97}Sb_{0.995}$ sample, which displayed an increase of dyscrasite (among others) compared to the former sample, but a smaller deviation of its lattice parameters, showing how a balance between the effect (and quantity) of secondary phases and intrinsic defects can impact the performance of a thermoelectric material, and may be achieved by a subtle tuning of the initial composition.

In fact, it is interesting to notice that there is a fine threshold where the amount of Ag in the nominal composition can impact the TE properties more than the Sb content,[26,31] which can be deduced from the similar TE behaviour of samples $MgAg_{0.965}Sb_{0.985}$ and $MgAg_{0.97}Sb_{0.995}$, but a distinctly different one of $MgAg_{0.955}Sb_{0.985}$. In this context, Mg-poor samples, with a lower Ag content, from $Ag_{0.965}$ to $Ag_{0.955}$ (a difference of ~1 at%), can lead to a decrease of the dyscrasite (Ag-rich) phase, while presenting along elemental Sb as a secondary phase, since it did not have a pair element to react with (Table 1). This was observed to be beneficial, leading to a lower increment in the charge carrier concentration and mobility, agreeing well with the studies from Camut *et al.*[24] and Liu *et al.*[22]

In summary, for this preparation route, the best composition was $MgAg_{0.955}Sb_{0.985}$, hitherto, for having a significantly larger electrical conductivity in comparison with others, while keeping a moderate Seebeck coefficient value, giving it a boost in the power factor, achieving $PF_{max} = 13.6\ \mu W\ K^{-2}\ cm^{-1}$ and an average value of 12.8 $\mu W\ K^{-2}\ cm^{-1}$, revealing a high performance throughout the whole temperature range. These can be attributed to the elemental Sb secondary phase and decrease of dyscrasite-Ag-rich, which agrees well with the study by Liu *et al.*[26]

Despite these values being lower than some of the best reported in the literature, the power factor, which is the pivotal parameter when designing a specific application requiring a particular power,[40] is still good. The overall performance may be enhanced by optimizing sintering conditions.

4. Conclusions

In this work, a novel synthesis route was developed for producing α-MgAgSb compounds, using induction melting, which can synthesise robust ingots, from raw pieces of the elements in a controlled atmosphere, in less than 10 minutes, followed by a 2 h sintering step to form 1 cm diameter pellets, testing three different compositions, $MgAg_{0.955}Sb_{0.985}$, $MgAg_{0.965}Sb_{0.985}$, $MgAg_{0.97}Sb_{0.995}$. The obtained samples exhibit a good power factor, achieving average values of 12.8 $\mu W\ K^{-2}\ cm^{-1}$ from 315 K to 525 K, for the composition $MgAg_{0.955}Sb_{0.985}$, which also shows that, depending on the synthesis and sintering routes chosen, the conventionally accepted $MgAg_{0.97}Sb_{0.995}$, with an average power factor of 8.8 $\mu W\ K^{-2}\ cm^{-1}$, might not always be the best choice.

By using this route, several advantages arise, such as a reduction in the number of steps during the fabrication of the sample, lessening the production cost, and noticeable shortening of the synthesis time. By using bulk elements instead of powder as precursors, the need for a glovebox is eliminated, as well as the health and environmental hazards that arise from the usage of powders. These make this process simpler and more appealing for industrial production conversion, thereby enabling it to reach the final markets more efficiently.

This production process led to the formation of secondary phases such as dyscrasite (Ag_3Sb) and elemental Sb, in the case of lower Ag concentration in the nominal composition. The formation interplay of Ag_{Mg} antisites and Ag vacancies, along with the presence of secondary phases in the samples, which create a complex interface network between the main matrix and these have a significant impact on the thermoelectric properties, by over-increasing the charge carrier concentration. These lead to a degenerated-like semiconductor behaviour, significantly deteriorating the charge carrier mobility through the insertion of grain boundaries and scattering centres.

Furthermore, this work demonstrated that the unwanted γ-phase may significantly decrease during the sintering step, despite its high presence after melting, as well as the diminishing of the Ag_3Sb secondary phases, thus demonstrating that the sintering step plays a crucial part in the thermoelectric performance.

In conclusion, using this novel route, the successful production of MgAgSb-based materials through induction melting followed by hot-pressing was demonstrated, significantly reducing the number of preparation steps, total time and complexity.

Author contributions

Beatriz A. Santos – conceptualization, investigation, formal analysis, methodology, visualization, writing – original draft; Ana I. de Sá – investigation; Paulo Luz – investigation; Filipe Neves – resources; Johannes de Boor – supervision, writing – review & editing; and António P. Gonçalves – resources, supervision, writing – review & editing.

Conflicts of interest

The authors declare no conflicts of interest.

Data availability

All experimental procedure is explained in detail in the main manuscript. Furthermore, the data supporting this article is available in the supplementary information (SI) document.

Supplementary information is available. See DOI: https://doi.org/10.1039/d5lf00400d.

Acknowledgements

This project was partially funded by the Fundação para Ciência e Tecnologia (FCT) through the projects PRT/BD/153039/2021 and UID/Multi/04349/2019. The authors would like to thank SUSTENET (CA24120) for their support.

Notes and references

1 J. He and T. M. Tritt, Advances in thermoelectric materials research: Looking back and moving forward, *Science*, 2017, **357**, eaak9997.

2 D. Sanin-Villa, Recent Developments in Thermoelectric Generation: A Review, *Sustainability*, 2022, **14**(24), 16821.

3 Q. Doraghi and H. Jouhara, Thermoelectric generator efficiency: An experimental and computational approach to analysing thermoelectric generator performance, *Therm. Sci. Eng. Prog.*, 2024, **55**, 102884.

4 G. J. Snyder and E. S. Toberer, Complex thermoelectric materials, *Nat. Mater.*, 2008, **7**, 105–114.

5 T. M. Tritt and M. A. Subramanian, Thermoelectric Materials, Phenomena, and Applications: A Bird's Eye View, *MRS Bull.*, 2006, **31**(3), 188–198.

6 A. Duparchy, *et al.*, Instability Mechanism in Thermoelectric Mg 2 (Si,Sn) and the Role of Mg Diffusion at Room Temperature, *Small Sci.*, 2025, **5**(3), 107874.

7 S. Twaha, J. Zhu, Y. Yan and B. Li, A comprehensive review of thermoelectric technology: Materials, applications, modelling and performance improvement, *Renewable Sustainable Energy Rev.*, 2016, **65**, 698–726.

8 D. Kusano and Y. Hori, Effects of PbTe Doping on the Thermoelectric Properties of (Bi2Te3)0.2(Sb2Te3)0.8, in *21st International Conference an Thermoelectronics (2002)*, 2002, vol. 2, pp. 13–16.

9 H. J. Goldsmid, Bismuth telluride and its alloys as materials for thermoelectric generation, *Materials*, 2014, **7**(4), 2577–2592.

10 Z. Ren, Y. Lan and Q. Zhang, *Advanced Thermoelectrics: Materials, Contacts, Devices, and Systems*, CRC Press (Taylor & Francis Group), 2017.

11 C. Y. Sheng, H. J. Liu, D. D. Fan, L. Cheng, J. Zhang, J. Wei, J. H. Liang, P. H. Jiang and J. Shi, Predicting the optimized thermoelectric performance of MgAgSb, *J. Appl. Phys.*, 2016, **119**(19), 195101.

12 M. J. Kirkham, A. M. Dos Santos, C. J. Rawn, E. Lara-Curzio, J. W. Sharp and A. J. Thompson, Ab initio

determination of crystal structures of the thermoelectric material MgAgSb, *Phys. Rev. B: Condens. Matter Mater. Phys.*, 2012, **85**(14), 1–7.

13 J. L. Mi, *et al.*, Elaborating the Crystal Structures of MgAgSb Thermoelectric Compound: Polymorphs and Atomic Disorders, *Chem. Mater.*, 2017, **29**(15), 6378–6388.

14 N. Oueldna, A. Portavoce, M. Bertoglio, A. Campos, A. Kammouni and K. Hoummada, Phase transitions in thermoelectric Mg-Ag-Sb thin films, *J. Alloys Compd.*, 2022, **900**, 163534.

15 S. Y. Yue, T. Xu and B. Liao, Ultralow thermal conductivity in a two-dimensional material due to surface-enhanced resonant bonding, *Mater. Today Phys.*, 2018, **7**, 89–95.

16 S. Lee, K. Esfarjani, T. Luo, J. Zhou, Z. Tian and G. Chen, Resonant bonding leads to low lattice thermal conductivity, *Nat. Commun.*, 2014, **5**, 1–8.

17 P. Ying, *et al.*, Hierarchical Chemical Bonds Contributing to the Intrinsically Low Thermal Conductivity in α-MgAgSb Thermoelectric Materials, *Adv. Funct. Mater.*, 2017, **27**(1), 1–8.

18 G. Li, *et al.*, Intrinsic mechanical behavior of MgAgSb thermoelectric material: An ab initio study, *J. Materiomics*, 2020, **6**(1), 24–32.

19 N. M. Ravindra, B. Jariwala, A. Bañobre and A. Maske, *Thermoelectrics: Fundamentals, Materials Selection, Properties, and Performance*, 2019.

20 J. Lei, D. Zhang, W. Guan, Z. Cheng, C. Wang and Y. Wang, Engineering electrical transport in α-MgAgSb to realize high performances near room temperature, *Phys. Chem. Chem. Phys.*, 2018, **20**(24), 16729–16735.

21 Z. Feng, *et al.*, Ag-Mg antisite defect induced high thermoelectric performance of α-MgAgSb, *Sci. Rep.*, 2017, **7**(1), 1–12.

22 Z. Liu, *et al.*, Understanding and manipulating the intrinsic point defect in α-MgAgSb for higher thermoelectric performance, *J. Mater. Chem. A*, 2016, **4**(43), 16834–16840.

23 Y. Liao, *et al.*, Sintering pressure as a 'scalpel' to enhance the thermoelectric performance of MgAgSb, *J. Mater. Chem. C*, 2022, **10**(9), 3360–3367.

24 J. Camut, I. Barber Rodriguez, H. Kamila, A. Cowley, R. Sottong, E. Mueller and J. de Boor, Insight on the interplay between synthesis conditions and thermoelectric properties of α-MgAgSb, *Materials*, 2019, **12**, 1857.

25 A. Duparchy, F. Kreps, E. Müller and J. de Boor, Unlocking the Full Potential of MgAgSb by Unravelling the Interrelation of Phase Constitution and Thermoelectric Properties, *Adv. Funct. Mater.*, 2025, **10200**, 1–16.

26 Z. Liu, *et al.*, Effects of antimony content in MgAg0.97Sbx on output power and energy conversion efficiency, *Acta Mater.*, 2016, **102**, 17–23.

27 X. Zhang, *et al.*, High-performance MgAgSb/Mg3(Sb,Bi)2-based thermoelectrics with η = 12% at T ≤ 583K, *Joule*, 2024, **8**(12), 3324–3335.

28 I. Rodriguez-Barber, J. Camut, L. Luhmann, A. Cowley, E. Mueller and J. de Boor, On the influence of AgMg precursor formation on MgAgSb microstructure and thermoelectric properties, *J. Alloys Compd.*, 2021, **860**, 158384.

29 S. E. Housh and J. S. Waltrip, Safe handling of magnesium alloys, *SAE Tech. Pap.*, 1990.

30 U. Nations, International Chemical Safety Cards (ICSCs) database, [Online], Available: https://chemicalsafety.ilo.org/dyn/icsc/showcard.listcards3?p_lang=en, [Accessed: 27-Jul-2025].

31 C. van Sice and J. Faludi, Comparing environmental impacts of metal additive manufacturing to conventional manufacturing, in *Proceedings of the International Conference on Engineering Design (ICED21)*, 2021, vol. 1, pp. 671–680.

32 S. Graulis, *et al.*, Crystallography Open Database - An open-access collection of crystal structures, *J. Appl. Crystallogr.*, 2009, **42**(4), 726–729.

33 H. Kopp, III. Investigations of the specific heat of solid bodies, *Philos. Trans. R. Soc. London*, 1865, **155**, 71–202.

34 T. Zhang, B. Dong and X. Wang, Optimization of the thermoelectric performance of α-MgAgSb-based materials by Zn-doping, *J. Mater. Sci.*, 2021, **56**(24), 13715–13722.

35 A. Duparchy, *et al.*, Establishing synthesis-composition-property relationships for enhanced and reproducible thermoelectric properties of MgAgSb, *J. Mater. Chem. A*, 2022, **10**(40), 21716–21726.

36 S. Y. Back, S. Meikle and T. Mori, Comprehensive study of α-MgAgSb: Microstructure, carrier transport properties, and thermoelectric performance under ball milling techniques, *J. Mater. Sci. Technol.*, 2025, **227**, 57–66.

37 J. Zhu, X. Zhang and M. Guo, *et al.*, Restructured single parabolic band model for quick analysis in thermoelectricity, *npj Comput. Mater.*, 2021, **7**, 116.

38 Y. Huang, J. Lei, H. Chen, Z. Zhou, H. Dong, S. Yang, H. Gao, T.-R. Wei, K. Zhao and X. Shi, Intrinsically high thermoelectric performance in near-room-temperature α-MgAgSb materials, *Acta Mater.*, 2023, **249**, 118847.

39 H. J. Goldsmid, *Introduction to Thermoelectricity*, Springer Berlin Heidelberg, Berlin, Heidelberg, 2nd edn, 2016.

40 A. Novitskii and T. Mori, Revisiting Pisarenko's formula: Effective mass estimation, thermopower–conductivity relation, and maximum power factor prediction, *Mater. Today Phys.*, 2025, **58**, 101845.